Research Square

Preprints are preliminary reports that have not undergone peer review.
They should not be considered conclusive, used to inform clinical practice,
or referenced by the media as validated information.

By-Layer Covalent Organic Structure as a Metal-Free PCET Catalyst for Efficient Oxygen Evolution in Alkaline and Neutral Media

Soheila Nakhjiri Kamrani
Razi University
Afshin Pashabadi
apashabadi@razi.ac.ir
Razi University
Mohammad Joshaghani
Razi University

Article

Keywords: PCET, Voltammetry, Proton relay, Oxygen evolution reaction, Porphyrin, OER

Posted Date: June 26th, 2026

DOI: https://doi.org/10.21203/rs.3.rs-10063880/v1

License: This work is licensed under a Creative Commons Attribution 4.0 International License.
Read Full License

Additional Declarations: No competing interests reported.

By-Layer Covalent Organic Structure as a Metal-Free PCET Catalyst for Efficient Oxygen Evolution in Alkaline and Neutral Media

Soheila Nakhjiri Kamrani[1,2] Afshin Pashabadi[1*] and Mohammad Joshaghani[1,2 *]

[1] Faculty of Chemistry, Razi University, Kermanshah, 67149-67346, Iran

[2] Nanoscience and Nanotechnology Research Center (NNRC), Razi University, Kermanshah, 67149-67346, Iran

✉ *Afshin Pashabadi

apashabadi@razi.ac.ir

✉ *Mohammad Joshaghani

mjoshaghani@razi.ac.ir

✉ Soheila Nakhjiri Kamrani

s.nakhjirikamrani@razi.ac.ir

ABSTRACT

The delayed evolution of proton transfer (PT) as the sluggish component of proton-coupled electron transfer (PCET) represents a critical limitation in the design of biomimetic artificial leaves. Here, we report a simple metal-free PCET catalyst for the oxygen evolution reaction (OER) operating in both neutral and alkaline media, realized through successive evolutionary stages of a bilayer covalent superstructure. Graphite/graphene oxide hosts a repetitive porphyrin-based covalent organic structure (COS) assembled via bidentate ethylenediamine (EDA) linkages, functioning as a PCET catalyst in both alkaline and neutral environments. The experimentally detected unusual Gerischer impedance signature demonstrates the overwhelming dominance of interfacial proton exchange over natural diffusion, revealing a distinct chemical electrochemical chemical reaction pathway in OER. The H/D isotope and proton inventory studies provide direct and compelling mechanistic insight. The results show a secondary isotope effect, confirming that O–H bond cleavage is not involved in the rate-determining step of the water oxidation reaction. For the first time, this study elucidates how a robust interfacial covalent organic structure (COS), acting as an in situ heterogeneous stimulus, actively reorganizes the hydrogen-bonding network of water. Reflective infrared spectroscopy unequivocally reveals the role of COS in disrupting and agitating interfacial hydrogen-bonded water clusters, liberating free water molecules and thereby promoting adsorption events during OER.

Keywords: PCET, Voltammetry, Proton relay, Oxygen evolution reaction, Porphyrin, OER.

1. Introduction

The precious and non-precious metal-based electrocatalysts have been frequently used to accelerate the oxygen evolution reaction (OER), the sluggish half-reaction of overall water splitting [1]. However, commercialization of water-splitting and Zn–air battery technologies remain severely limited by the high cost, poor durability, and environmental concerns associated with metal-based catalysts. On the other hand, PCET imbalance between electron transfer (ET) and proton transfer (PT) represents an intrinsic bottleneck in OER electrocatalysis [2, 3], necessitating the incorporation of external proton acceptors or solution bases, whose operation is constrained by slow diffusion kinetics within the interfacial diffusion layer and catalyst instability under harsh reaction conditions. Additionally, “redox leveling” enables access to high oxidation states within a limited potential window through facile deprotonation. Meanwhile, retarded “water delivery” and inefficient “proton shuttling” to and from the current collector may induce incomplete water oxidation pathways and generate reactive oxygen species (ROS), such as OH•, which progressively degrade catalyst frameworks [4]. These limitations represent major challenges in establishing a holistic design blueprint for bioinspired artificial leaves capable of rivaling the oxygen-evolving complex (OEC) of photosystem II (PSII) in molecular oxygen production [4]. The key function of OEC in PSII lies in the spatial delocalization and dynamic management of protonic species (H^+ and H_2O), preventing proton accumulation while ensuring efficient delivery of water substrates [5, 6]. Recent structural studies have provided profound insight into the three-dimensional proton-transport networks surrounding the $CaMn_4O_5$ active core of OEC [5, 7].

Recently, we synthesized a guanidinium-terminated polymeric interface [2] and the first single-crystalline zwitterionic hydrogen-bonded framework (ZHOF) extended in two dimensions via strong Speakman-type hydrogen bonding [3] as metal-free PCET catalysts (proton relays) for enhancing OER. Zhang et al. fabricated a heteroatom-doped (N and P) mesoporous carbon-foam electrocatalyst for oxygen reduction and evolution reactions [1]. According to Sabatier’s principle, functional groups capable of PT can act as proton conveyors to and from the catalytic nerve center of PCET systems [8]. Accordingly, the most effective strategy involves clustering basic residues in close

proximity to reinforce Grotthuss-type proton hopping pathways, thereby accelerating interfacial proton transport [9].

Graphene oxide substrate (GO) can be one of the green candidates for extending low-cost metal-free platform tailoring in PCET electrocatalysts because of its facile reactivity, stability in harsh medium, and functionalization through different electro-/chemical conditions. It includes oxygenated functional groups such as epoxy, hydroxyl, and carboxyl groups, which can easily be functionalized with other organic structures through covalent bonding suitable in harsh OER conditions [10-12]. Porphyrin-based organic superstructures have received increasing attention in phot-/electrochemical catalysis [13-15]. For example, a copolymer of porphyrin with terephthaloyl was synthesized and employed as a water-splitting electrocatalyst, although no experimental proof described the details of the PCET mechanism and propulsion of heterogeneous reaction [14]. Based on our recent OER proton-relay studies, it is found that fabricating biomimetic 3D arrangement of organic base and superbases is a key event to accelerate the proton hopping mechanism. In this way, one of the promising superstructures is covalent organic structures (COSs) a type of porous organic superstructures that contain light elements (B, C, N, O, etc.) and are covalently connected through these porphyrin sub-units and give high chemical stability, plentiful active sites, donor heteroatoms (N and O), π-conjugated conducting skeleton, and higher specific surface area [16].

In this work, we present the synthesis of a metal-free porphyrin-based by-layer covalent organic structure (COS) as a PCET catalyst for OER. The structure was synthesized using 5,10,15,20-tetrakis-(4-hydroxyphenyl)-porphyrin (THPP) and ethylene diamine (EDA) through a repeated AA pattern via the aliphatic covalent linkages on graphene oxide (GO). It was subjected to explore the possible promotion of the sluggish part of PCET, PT, during OER in both pH-dependent and pH-neutral solutions. The attachment EDA through methyl bromoacetate (MBA) linkages along two ascending layers of COS endows a proliferation of amine per-tecton and the acceleration of the PCET process. We unveil the undeniable role of the focal pyrrolic amines on proton hopping, where the inclusion of Mg fully aborted the OER activity in a neutral medium. Using D/H kinetic isotopic effect and proton inventory studies, we track the kinetic and details of COS in OER and more generally provide a strategy to probe fundamental PCET mechanisms by

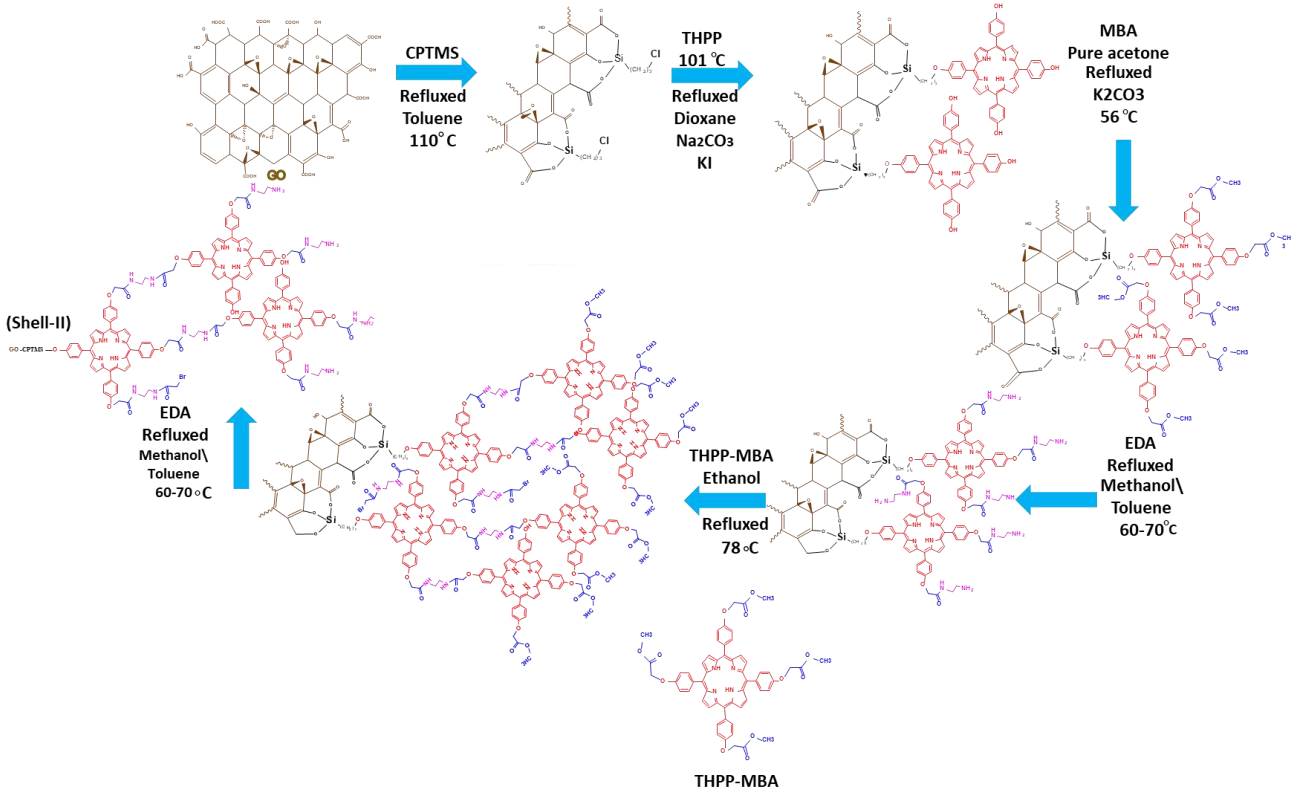
covalent structures using isotopic studies. Gersicher impedance appearance in high frequency domain conveys the outstanding role of COS in regulating PCET during OER so that the natural diffusion of protonic species to/from the current collector is practically blocked, a chemical-electrochemical-chemical mechanism. Using reflective infrared spectroscopy, we studied the interfacial agitation of water's hydrogen bond network by COS, where the deliverance of free water molecules may endow further succeeded adsorption events and regulate heterogeneous WOR. The GO-COS with tow layer of THPP-EDA (Shell-II) displays an outstanding catalytic performance with a current density of 100 mA cm^{-2} in overpotential ca. 0.49 V and an onset potential of 1.72 *vs*. reversible hydrogen electrode (RHE) in 1.0 M of KOH with remarkable resistance and stability in different ranges of pHs.

2. Results and discussion

2.1. Characterization

The as-prepared electrodes GO, GO-(3-Chloropropyl trimethoxysilane (CPTMS)), GO-CPTMS-THPP, GO-CPTMS-THPP-MBA, GO-CPTMS-THPP-MBA-EDA (Shell-I), (Shell-I)-MBA-THPP-MBA, and (Shell-I)-MBA-THPP-MBA-EDA (Shell-II) were characterized and employed for WOR studies. Complete information on the fabrication methodology of all electrodes is provided in the Supporting Information (SI). Initially, CPTMS-grafted graphene oxide (GO-CPTMS) was prepared via nucleophilic substitution of GO with CPTMS linkers. The obtained GO-CPTMS was subsequently coupled with THPP to yield GO-CPTMS-THPP. The resulting GO-CPTMS-THPP was then modified with methyl bromoacetate (MBA) in anhydrous acetone containing K_2CO_3 as a base catalyst to produce GO-CPTMS-THPP-MBA. The amide-linked GO-CPTMS-THPP-MBA-EDA (Shell-I) was obtained through reaction of ethylenediamine (EDA) with terminal acetate groups [17]. Repeating the THPP and EDA coupling sequence generated a well-defined bilayer superstructure that significantly enhances WOR activity. Scheme 1 illustrates the schematic construction of the electrodes, demonstrating synthesis of a new class of GO-THPP-EDA bilayer arrays. Energy-dispersive X-ray analysis (EDXA), employed for surface elemental analysis and chemical characterization, is shown in Figures S3–S9.

During electrode fabrication, EDXA spectra collected after each modification step confirm the presence of the targeted elements within the evolving structural framework.



Scheme 1. The schematic of the fabrication of by-layer repetitive GO-THPP-EDA electrode

The FT-IR results confirm the stepwise structural modification of the GO electrode, with the appearance of characteristic functional groups at each stage, as shown in Fig. 1A–G. In the FT-IR spectrum of the GO electrode (Fig. 1A), a strong and broad band centered at 3375 cm^{-1} is assigned to the stretching vibration of hydroxy functional groups on GO and lattice water molecules. The band at 1719 cm^{-1} can be related to the C=O vibration of carboxy and carbonyl groups. The band at 1619 cm^{-1} can be attributed to the skeletal vibration of C=C in graphene sheets, confirming the sp^2-hybridized carbon skeleton. The band at 1380 cm^{-1} may be assigned to C–C bond vibrations, confirming surface defects. The relative intensity ratio of v(C=C) {1619}/v(C–C) {1380} is consistent with a relatively high oxidation degree [18]. The observed peak at 1032 cm^{-1} is related to C–O stretching of hydroxy and epoxy groups. The relative intensity of v(C=O) at 1719 cm^{-1} is significantly

lower than that of v(C–O) at 1032 cm^{-1}, indicating that hydroxy and epoxy groups are the dominant oxygen-containing functionalities on GO [18, 19].

In the FT-IR spectrum of GO-CPTMS shown in Fig. 1B, the bands at 1090 and 1220 cm^{-1} can be collectively attributed to Si–C stretching vibrations. The bands at 1230 and 1300 cm^{-1} are related to C–Cl stretching. Additionally, the bands at 470 and 475 cm^{-1} correspond to Si–O bending vibrations. The FT-IR spectrum of free THPP is shown in Figure S11. The band at 3415 cm^{-1} is assigned to –OH stretching of the THPP ring, while the band at 3317 cm^{-1} corresponds to N–H stretching of THPP. C–N bending appears at 798 cm^{-1}, and the bands at 1000 and 1350 cm^{-1} are attributed to C–N stretching vibrations of THPP. The emerging peaks at 1500 and 1660 cm^{-1} are related to C=C stretching. The bands appearing at 1000 and 1260 cm^{-1} are assigned to C–O vibrations of THPP.

Upon binding THPP to CPTMS, the GO-CPTMS-THPP electrode was obtained, and its FT-IR spectrum (Fig. 1C) displays all characteristic bands of the constituent components. The FT-IR spectrum of GO-CPTMS-THPP-MBA is shown in Fig. 1D. The bands at 1736 and 1200 cm^{-1} are mainly assigned to C=O and C–O stretching of MBA. An additional band at 612 cm^{-1} can be attributed to C–H out-of-plane and in-plane bending vibrations of the benzene moiety in the porphyrin ring.

Figure 1E shows the FT-IR spectrum of the Shell-I electrode. Changes in the region of 3300–3500 cm^{-1} can be assigned to the presence of N–H stretching vibrations. N–H bending appears at 1560–1640 cm^{-1}, C–N stretching is observed at 1000–1350 cm^{-1}, and the band at 1617 cm^{-1} is assigned to C=O stretching of the amide group. The FT-IR spectrum of (Shell-I)-MBA in Fig. 1F shows that, upon addition of MBA to the first-layer structure, the N–H stretching band disappears, while the C=O stretching band of MBA reappears. This behavior indicates successful progression of the reaction and coupling of MBA with EDA.

Finally, the FT-IR spectrum of Shell-II in Fig. 1G shows that, upon addition of EDA to the previous electrode, the N–H stretching band reappears and the C=O stretching of MBA shifts to lower wavenumber, confirming construction of the final multilayer electrode architecture [20].

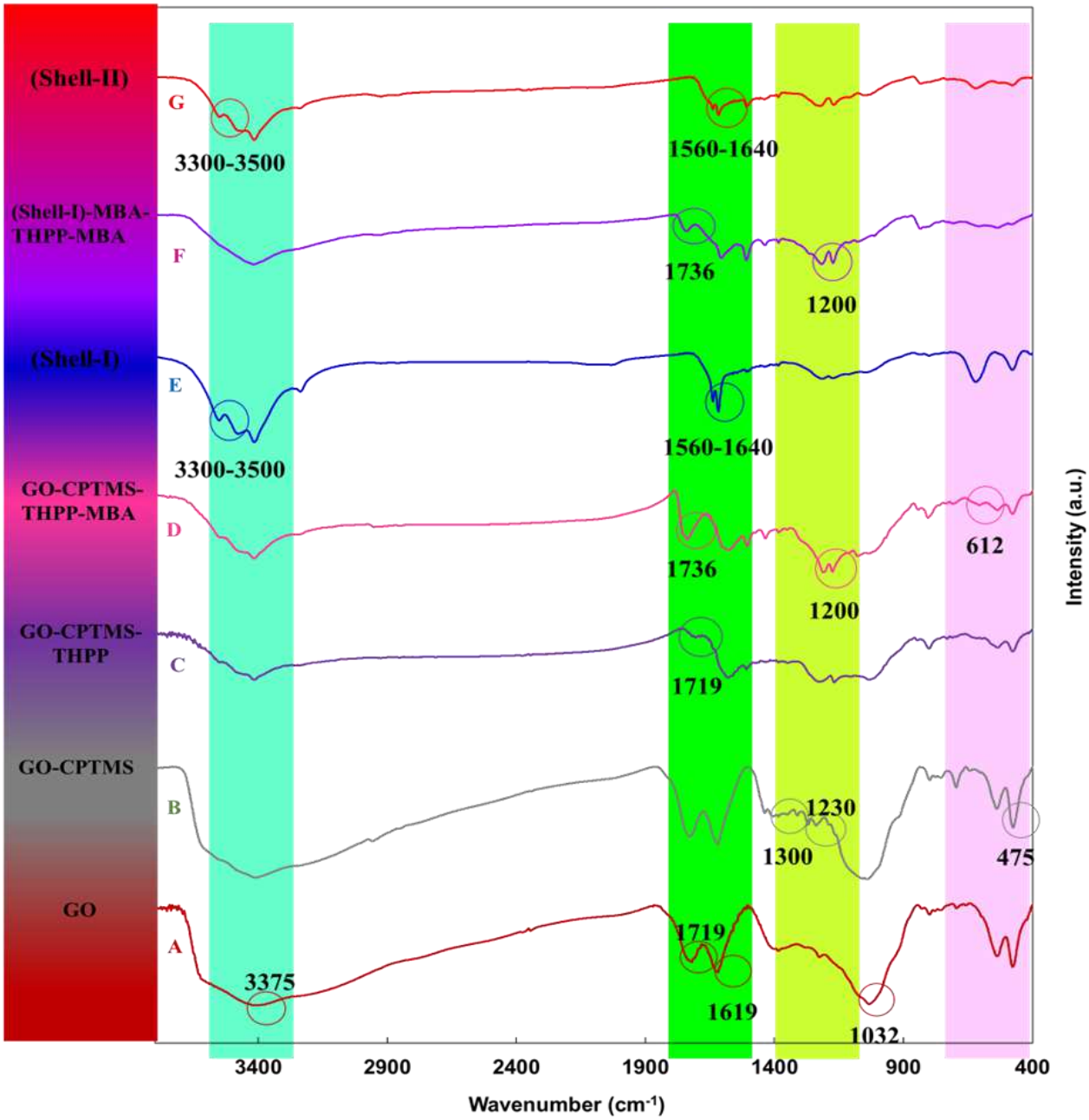


Fig. 1. FT-IR spectra of electrodes: (A) GO, (B) GO-CPTMS, (C) GO-CPTMS-THPP, (D) GO-CPTMS-THPP-MBA, (E) Shell-I, (F) (Shell-I)-MBA-THPP-MBA and (G) Shell-II.

The ^{1}H-NMR spectrum (500 MHz, in DMSO) of THPP substance shown in (Figure S13) includes signals at: δ=-2.94 (s, 2H) for N-H protons, 7.23 (d, J = 8.4 Hz, 8H, Ar-H) and 8.00 (d, J = 8.4 Hz, 8H, Ar-H). Peak at 8.83 (s, 8H) is assigned for Pyrrole-H protons and signal at 9.96 (s, 4H) is due to Ar-OH protons [21]. The ^{1}H-NMR spectrum of THPP-MBA in (Figure S14) demonstrates signals at δ= -2.94 (s, 2H) for protons of N-H group, 3.81

(br, 12H) for O-CH_3 protons, 5.1 (br, 8H) for protons of CH_2-O group and 7.4 (br, 24H) for aryl and pyrrole protons. The ^{1}H-NMR spectrum of THPP-MBA-EDA in (Figure S15) (400 MHz, in $CDCl_3$) reveals: signals related to N-H group at -2.94 (s, 2H), 1.3 (br, 8H) for NH_2 and 3.88 (m, 16H) for protons of CH_2-NH_2 group, 5.1 (s, 8H) for CH_2–O protons, 5.2 (s, 8H) also for NH_2 group and 7.3 (br, 24H) for aryl and pyrrole protons. The ^{1}H-NMR spectrum of THPP-MBA-EDA-MBA-THPP-MBA in (Figure S16) (400 MHz, in DMSO) shows: signals at -2.94 (s, 10H) and 1.4 (br, 8H) related to N-H group, 2.5 (m, 16H) for CH_2 –NH protons, 3.81 (br, 36H) for protons of O-CH_3 group, 3.99 (br, 12H) for CH_2-NH_2 protons, 5.1 (s, 40H) for CH_2–O group and 7.08 (br, 64H), 7.4 (br, 8H) and 8.23 (br, 8H) for aromatic protons and 8.99 (br, 40H) for pyrrole protons. The ^{1}H-NMR spectrum of THPP-MBA-EDA-MBA-THPP-MBA-EDA in (Figure S17) (400 MHz, in DMSO) shows: signal at δ= 1.4 (br, 20H) for NH group, 2.5 (m, 40H) for CH_2 –NH protons, 3.99 (br, 48H) for CH_2-NH_2 protons, 5.1 (s, 40H) for CH_2–O protons, 7.08 (br, 64H), 7.4 (br, 8H) and 8.23 (br, 8H) for aromatic protons and signal of 8.99 (br, 40H) for pyrrole protons [17].

The degree of freedom of water molecules involved in the hydrogen-bonded (HB) water clusters, which predominates the interfacial adsorption efficiency of the water molecules, can be directly boosted through strong interfacial agitating of the surface bonded COS. In 2018, our research group established a comprehensive experimental and theoretical study on the role of perturbation of water clusters through ultrasound irradiation an equivalent effect on heterogeneous WOR [22]. Herewith for the first time, we investigate the impact of the robust interfacial covalent structure, in situ heterogeneous stimuli, on water's hydrogen bonds (HBs) network, where successful adsorption events of protonic species can be controlled. Using attenuated total reflection infrared spectroscopy (ATR-IR), we compare water OH-stretching bond broadened on 2800-3700 cm^{-1} employed to consider the possible role of extensive HB agitation by by-layer COS. After recording the IR spectra for Graphite GR+water and GO/COS+water, the OH-stretching bands were deconvoluted to the four sub-bands of water denoted to the multiple degree of HBs modes [23, 24]. Fig. 2 shows the results of the curve-fitting analysis of the FTIR spectra for GR+water (A) and GO/COS+water (B). The resolved spectra displayed four peaks from *ca.* 3400 cm^{-1} to 3600 cm^{-1} corresponding to triply, doubly, singly and free (non-hydrogen bonded) hydrogen-bonded H_2O, respectively [22, 25]. The degree of breaking HBs

network (DBHB), as the ratio of calculated peak area of free water spectra (the green curve) around 3400 cm^{-1} to that of the hydrogen-bonded water molecules around 3600 cm^{-1} (blue curve), were respectively found to be as $\frac{0.0854}{0.6240} = 13.71\%$ at plot A (GR+W) and $\frac{0.1070}{0.5930} = 18.05\%$ at plot B (GO/COS+water). The increased DBHB for GO/COS+water compared to GR+W conveyed the increase of deliverance of a free water molecule, which can directly improve successful adsorption events during heterogeneous WOR [22, 26].

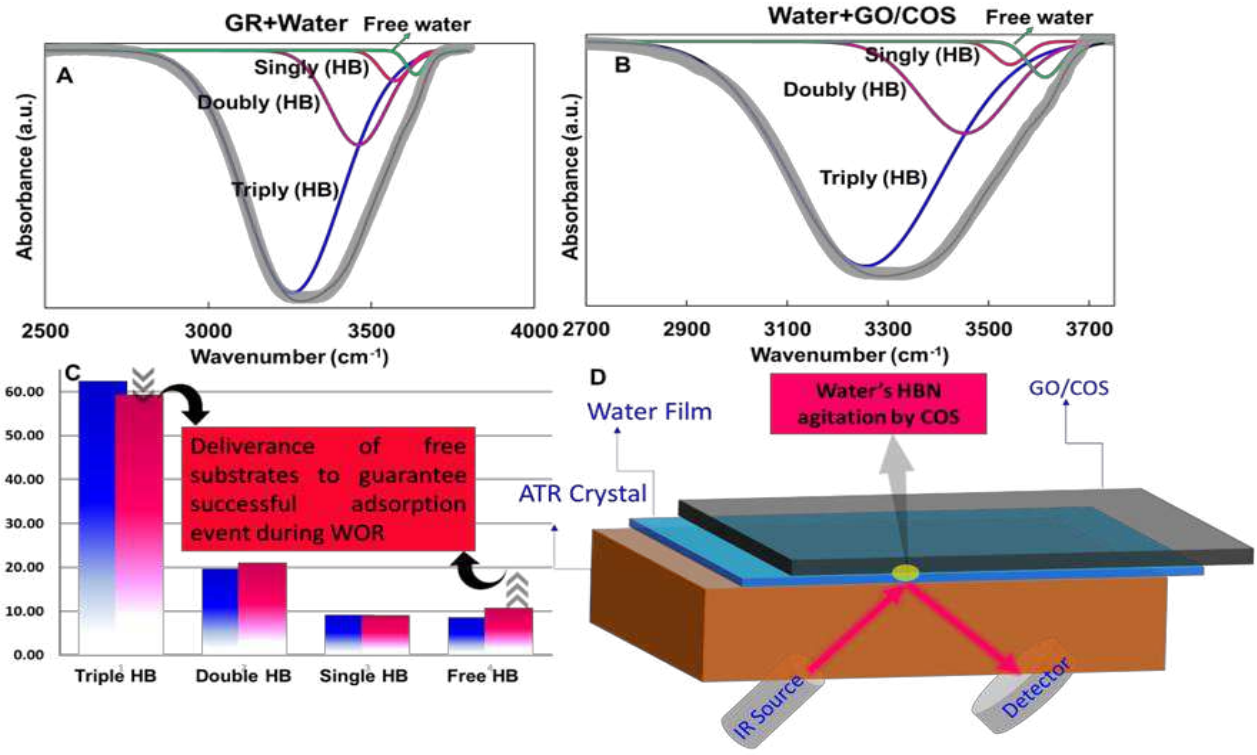


Fig. 2. The OH-stretching IR band (thick) and its Gaussian components (thin) for GR+Water (A) and GO/COS+Water (B). The plots show the experimental line shape (transparent black), curve fit (black), and four resolved components blue, purple, pink and green, corresponding to OH stretching of H-bonded water aggregates with cluster numbers of 3, 2, 1 and non-H-bonded bonded water, respectively. The peak area of the blue and green curves after treatment with COS decreased and increased respectively (C). Schematic of ATR experiment undertaken to explore the interfacial agitation of water's HB (D).

2.2. Electrochemical studies

The as-prepared electrodes were utilized as the working electrode in a standard three-electrode configuration to track their principal activity as a PCET catalyst against WOR in both alkaline and neutral media. The relevant polarization curves were recorded in 0.1 M

KOH (Figure S18), 1 and 3 M of KOH and also in a buffered solution (pH≈7) at 5 mV s^{-1} (Fig. 3). All the measured potentials were reported as RHE ($E_{RHE} = E_{Ag/Agcl} + 0.059\ pH + 0.198$ V). Fig. 3A and B compare the resultant linear sweep voltammograms (LSVs) possessed respectively in 3 and 1 M of KOH on the different stages of evolution of the graphite rod/GO-based COS. The prominent catalytic activity with the highest current density values were obtained for Shell-I and Shell-II. At first glance, the LSVs taken from all electrodes in 3 M KOH exhibit lower overpotentials discrepancy compared to 1 M of KOH having lower driving force. GR and GO show the same catalytic activity at 3 M of KOH, while display an apparent separation at a lower driving force of KOH 1 M. The overpotential discrepancy at 50 mA cm^{-2} was found to be 28 mV (in 3 M KOH) and 74 mV (in 1 M KOH) between Shell-I and Shell-II. An anodic shoulder corresponding to the porphyrin N–H/N• redox couple is clearly observed in Shell-I, attributable to direct electrolyte access and minimal electronic perturbation. In contrast, this feature is markedly attenuated in Shell-II, likely due to partial shielding by the upper porphyrin layer, increased electron-tunneling distance to the electrode [27], and enhanced π-delocalization across the bilayer architecture [28], which collectively suppress the discrete faradaic response. The overpotential 449 mV at 50 mA cm^{-2} in 1 M of KOH is lower than the value 595 mV possessed for the nickel foam/Co-LDH as an atypical electrocatalyst for OER in the basic medium [29]. Shell-II demonstrates a η@100 mA cm^{-2} at 398 m V that was just 99 mV higher than one of the strongest transition-metal hybridized electrocatalysts recently designed in our groups [29]. Figure S18 where the corresponding overpotentials at a fixed current density decrease in the order: GO < Shell-I < Shell-II. The examination of the catalytic performance of Shell-II at neutral pH reveals a significant negative shift compared to GR, GO, and Shell-I (Fig. 3C). The neutral activity of COS provides compelling evidence for efficient PT within this bilayer metal-free superstructure. This observation is particularly significant considering that, under neutral conditions, the accumulation of surface-generated protons may severely impede catalytic turnover. The overpotential required to achieve J = 10 mA cm^{-2} was determined to be 607 mV at pH ≈ 7. The overpotential was reduced by 502 mV relative to GR for J = 0.9 mA cm^{-2} under neutral conditions. Notably, catalytic activity is completely suppressed upon inclusion of Mg as a non-electroactive metal cation, such that the current density drops

to values comparable to GR. This Mg effect highlights the critical role of the four interconnected pyrrole units (focal amines), which possess strong metal-binding affinity, in mediating proton shuttling during OER.

The Tafel slopes at GO-CPTMS-THPP, Shell-I, (Shell-I)-MBA-THPP-MBA, and Shell-II under pseudo-polarized conditions were calculated to be 226, 207, 165, and 123 mV dec^{-1}, respectively. These results demonstrate a successive decrease in Tafel slope with increasing covalent superstructure complexity, indicating progressive acceleration of the oxidation reaction upon sequential incorporation of porphyrin and EDA moieties (Fig. 3D). A brief derivation of the Tafel slope based on the expression $2.303RT/(\alpha + n)F$, where n represents the number of ET steps preceding the rate-determining step and α is assumed to be 0.5, consistent with the theoretical slope of 118 mV dec^{-1}, suggests n = 0, indicating the absence of electron transfer prior to the RDS in the water oxidation reaction [31, 32]. Accordingly, it can be inferred that the first ET step of heterogeneous OER constitutes the RDS. Conversely, if the second ET step were rate-limiting, the expected Tafel slope would be approximately 40 mV dec^{-1} [2, 30]. The Faradaic efficiency was evaluated under constant current electrolysis at 0.008 A in 1 M KOH and the corresponding result was found to be 94.6% (Fig. 3E). The sustained stability and negligible current decay over prolonged operation indicate a high charge-to-oxygen conversion efficiency, consistent with the preserved catalytic architecture and efficient PCET mechanism observed in the bilayer COS framework.

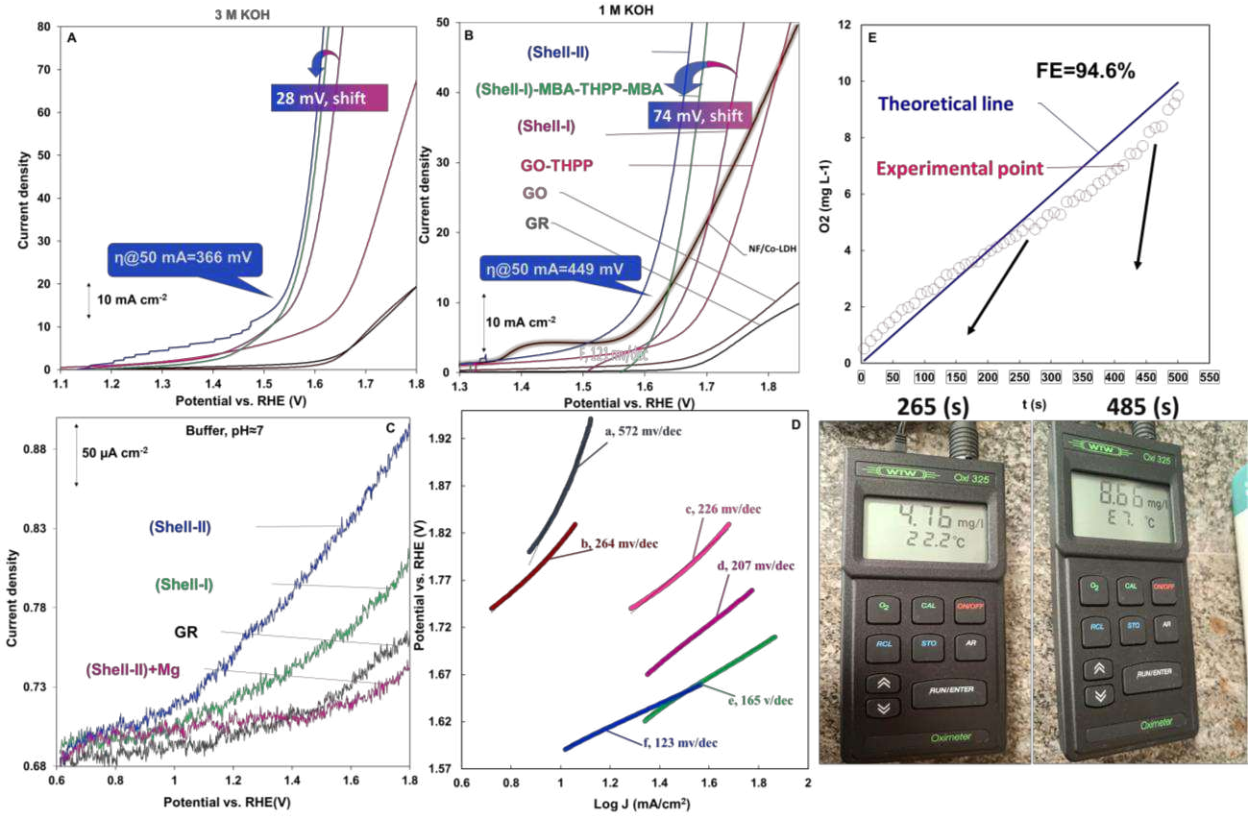


Fig. 3. Electrochemical assessments of WOR on the as-prepared electrodes. (A) and (B) Linear sweep voltammetry (LSV) curves with a scan rate of 0.01 V/s in 1 and 3 M of KOH and (C) The equivalent Tafel plots obtained from the current densities reported (J = 100 mA/cm^2), at a) GR, b) GO, c) GO-CPTMS-THPP, d) Shell-I, e) (Shell-I)-MBA-THPP-MBA, f) Shell-II. The lowest Tafel plot of 123 mV/dec was obtained for by-layer structure of the Shell-II electrode, where, the contribution of the EDA and THPP parts intensely increase the OER kinetics. E) Faradaic efficiency (FE) for Shell-II was evaluated under chronopotentiometry conditions at a constant current of 0.008 A in 1 M KOH. Correlation of oxygen evolution (Pink point curve) with the charge passed through the electrode system (the blue line corresponds to 100% Faradaic efficiency).

2.3. Kinetic isotope effect

Deuterium/proton kinetic isotope effect studies (KIEs) were conducted to estimate the efficiency of PT within the PCET process and to assess the dependence of the rate-determining step (RDS) of OER on ET versus PT. Theoretically, KIE is calculated from the ratio of rate constants (K_{H_2O}/K_{D_2O}), which are respectively proportional to J–H_2O and J–D_2O (see Supporting Note 1). A primary KIE (PKIE), defined as a KIE value larger than 1.5, indicates that PT occurs at the RDS or at least in one of the steps affecting the kinetics of PCET. In contrast, KIE values < 1.5 (secondary KIE, SKIE) suggest no significant PT involvement in the RDS [3, 26, 31]. The electrochemical tests were conducted by recording LSV plots in H_2O and D_2O media at equivalent basic pH(D), where the pD value

was calculated using the equation pH_{read} + 0.41 = pD. KOH and K_3PO_4 basic solutions were used to adjust pH or pD values in the H_2O and D_2O media.

Figure 4A–H respectively present voltammograms obtained on graphite (A), GO (B), GO-CPTMS-THPP (C), GO-CPTMS-THPP-Mg (D), Shell-I (E), (Shell-I)-MBA-THPP-MBA (F), Shell-II (G), and (Shell-II)-Mg (H) in H_2O (blue curves) and D_2O (pink curves) solutions. As shown, GO and GO-CPTMS-THPP exhibit distinct activities in proteo and deutero solutions, indicating a primary kinetic isotope effect (PKIE) ranging from ca. 3.8 to 2.0. The gradual evolution of the organic structure, achieved exclusively through covalent linkages between THPP and ethylenediamine, results in the formation of Shell-I and Shell-II with a dramatic improvement in PCET characteristics, such that Figures 4C–F illustrate near overlap of current densities in proteo and deutero solutions, falling within the SKIE regime (KIE < 1.5) [2, 3].

The large PKIE observed in plots A and B reflects a more symmetric transition state, whereas the secondary KIE displayed in other COS systems points to a more asymmetric transition state. The primary parameters influencing the magnitude of KIE and PCET kinetics are the zero-point energy and the overlap of vibrational wave functions, which are directly correlated with H-bonding efficiency and proton donor–acceptor proximity [3, 32]. The strength of the HB between donor and acceptor was estimated through the small fractionation factor (φ), as evaluated in the proton inventory studies (see the following section).

The insets of Figure 4 display the potential dependence of KIE values and show a slight increase in KIE with increasing overpotential. The lag of J_D at higher overpotentials may arise from a slightly delayed PT for O–D relative to O–H as the driving force (ET rate) increases. Beyond a specific energy threshold, this discrepancy becomes apparent and the voltammograms diverge, as the shorter O–D bond length is energetically less favorable for PCET than the O–H bond. Figures 4C and 4D compare the influence of Mg inclusion on PT behavior and reveal a KIE reversal of up to 25%. As supported by UV–Vis spectra (upon Mg inclusion, Figure S12), this variation originates from the synergistic role of focal amines in the overall proton-hopping mechanism [33]. A similar role of covalently attached EDA is observed in Figures 4E and 4G, where no detectable

discrimination is observed in H/D isotopic studies, indicating that no substantial O–H bond cleavage is directly involved in the RDS of OER.

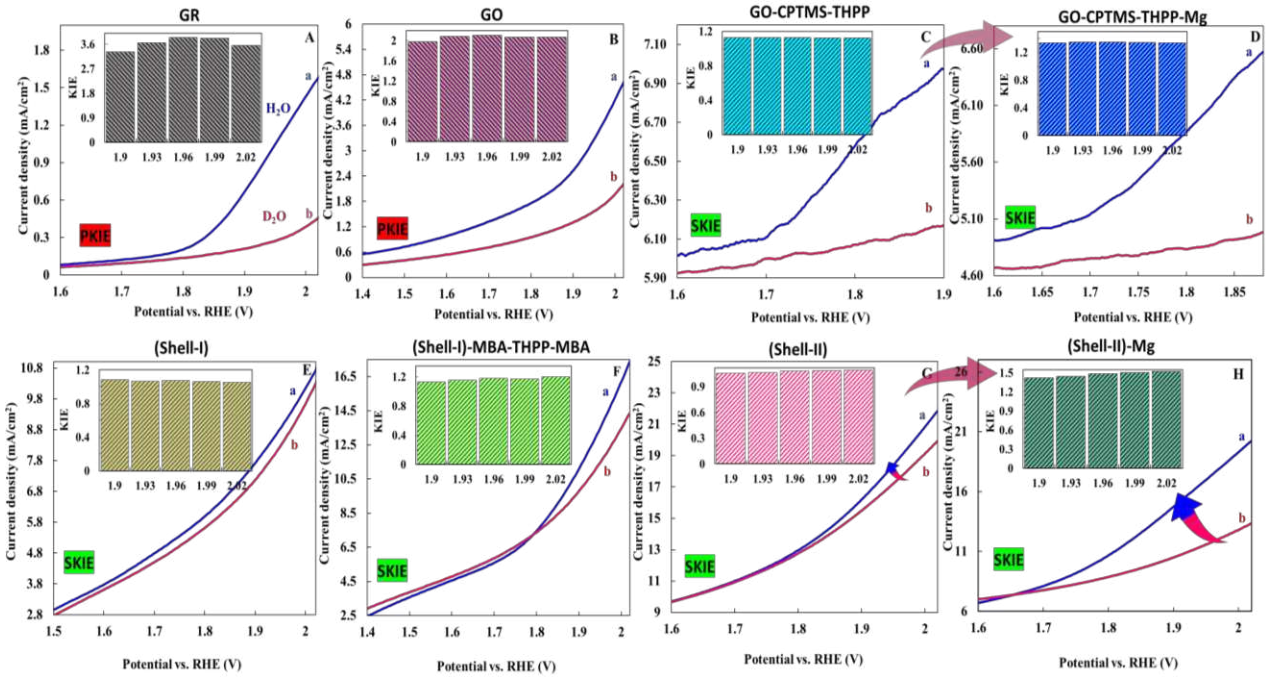


Fig. 4. Kinetic isotopic effect studies on different electrodes as a proton relay for OER reaction. The LSVs recorded in H_2O (blue curves) and D_2O (red curves) at (A) (GR), (B) GO, (C) GO-CPTMS-THPP, (D) GO-CPTMS-THPP-Mg, (E) Shell-I, (F) (Shell-I)-MBA-THPP-MBA, (G) Shell-II and (H) (Shell-II)-Mg.

2.4. Proton inventory studies

A higher dissociation energy and lower zero-point energy of the O–D bond in D_2O led to higher activation energy for bond cleavage upon isotopic substitution. The vibrational wave function and its overlap play a central role in determining the reaction rate and modulating the KIE of PCET reactions. Therefore, in the final evolution stages of bilayer COS (Shell-I and Shell-II), EDA placement induces enhanced orbital overlap between proton donor and acceptor sites (maximized proximity), thereby reducing the PT distance and facilitating efficient proton hopping [2, 34]. Following the KIE studies, the number of active protonic sites contributing to the catalytic process was further evaluated through proton inventory (PI) as a quantitative form of solvent isotope effect. PI has been extensively applied in enzymology to track the kinetics of PT to and from a catalyst's active center [34]. The relationship between OER activity and partial deuteration of water molecules can elucidate the degree of PT concertedness and the involvement of multiple proton-transfer events [2, 3, 31]. Figure 5 presents the LSVs (A, C, and E) and

corresponding PI plots of J_n/JH versus the mole fraction (n) of D_2O (B, D, and F) in D_2O/H_2O mixtures for GR, Shell-I, and Shell-II, respectively. As shown, the obtained J values during gradual deuteration are plotted against n-D_2O to track how the rate constant (k ≈ j; see SI Note 1) systematically evolves with increasing D_2O mole fraction. The experimental dotted plots were fitted using a modified Kresge–Gross–Butler equation to extract mechanistic parameters governing proton participation, as follows [2, 9, 35, 36].

$$j_n = j_0[1 - n + n\phi]Z^n$$

Here, J_n and J_0 are the current densities in H_2O and in different mole fractions of D_2O in H_2O, respectively. The symbol ϕ defines the isotopic fractionation factor, i.e., the deuterium preference of hydrogenic sites in the reactant or transition state relative to that of the water molecule (reflecting relative partitioning of D and H between coexisting phases). The total isotopic effect arising from many equivalent hydrogen sites is quantified by the Z-effect, also known as Z-sites. Z, or the Z-effect, measures a combination of individual weak isotope effects originating from multiple equivalent hydrogenic sites (Supporting Note 2). The magnitude of ϕ directly depends on the adjacent vibrational functions of isotopic sites and thus serves as a criterion for HB strength [2, 9, 35]. A non-linear propensity implies a proton-shuttling process and suggests the participation of multiple sites in the isotope effect, whereas a linear dependence demonstrates the presence of a single dominant site in the KIE [2, 3, 34, 35].

Figure 5B illustrates linear behavior fitted with the established equation $J_n/J_0 = 1 - n + 0.33n$, indicating a transition state stabilized by a single protonic interaction [2, 35]. In contrast, fitting of Figures 5D and 5F with non-linear dome-shaped curves yields coupled ϕ–Z values of 0.284–1.492 for Shell-I and 0.228–1.611 for Shell-II, respectively. Values of ϕ < 0.25 have previously been reported for single-well potential energy diagrams (Figure S19), consistent with potential flattening and low-frequency vibrational modes (low zero-point energy) governing H transport [2, 31, 34, 36, 37]. The decrease in ϕ from 0.284 to 0.228 highlights the pronounced effect of bilayer COS extension from Shell-I to Shell-II on the proton-hopping mechanism. Simultaneously, the increase in Z from 1.492 to 1.611 implies an enhanced aggregate inverse isotope effect at the COS active sites. The boundary condition of ϕ (< 0.25) corroborates the strongest mode of H-bonding (Figure

S19); therefore, the zero-point energies of H and D in O/H/N (N terminals in COS) and O/D/N transitions remain higher than the corresponding energy barriers [2].

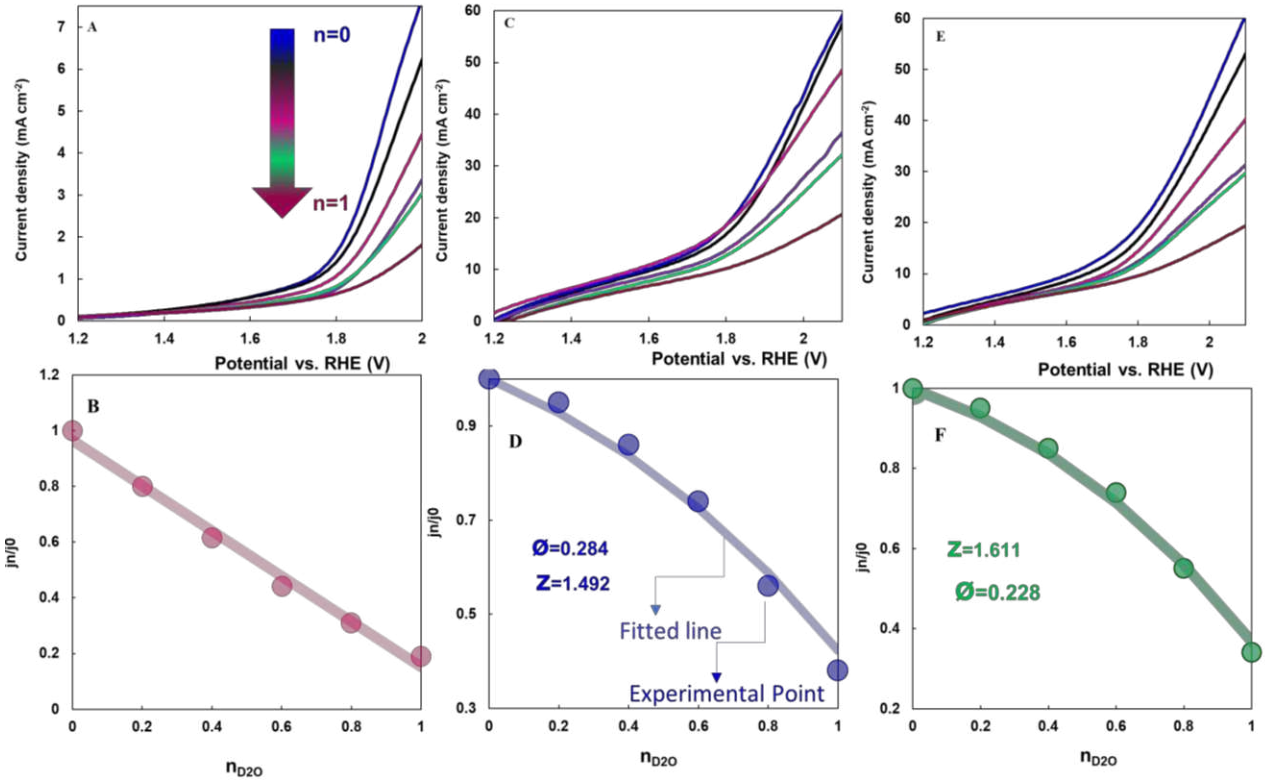


Fig. 5. Proton inventory and atom proton transfer studies. LSV curves of (A) GR, (C) Shell-I and (E) Shell-II in H_2O, D_2O and mol fractions ratio of [D]/([D]+ [H]) (n) at a potential 1-2.1 on the RHE scale. Plots of J_n/J_0 vs. mole fraction of D_2O in H_2O and fitting curves, the related parameters (ϕ and Z) at (B) GR, (D) Shell-I and (F) Shell-II shown in order.

In conclusion, the results of PI indicate that the hopping mechanism is directly governed by the synergistic role of amine groups through the strongest type of H-bonding. We did not consider a significant contribution from isotope effects originating from reaction intermediates or other functional groups in the covalent structure with relatively weaker H-bond interactions, small KIE, and $\phi \approx 1$, which therefore do not substantially contribute to the overall isotope effect. The additional data obtained at different overpotentials are summarized in Table 1 (the corresponding plots are shown in Figures S20–S23 at potentials of 1.7, 1.8, 1.9, and 2 V vs RHE).

Table 1. The results of PI calculation at the Shell-II electrode

Potential vs RHE	ϕ	Z
1.7	0.380	1.390
1.8	0.331	1.392
1.9	0.300	1.399
2	0.229	1.401
2.1	0.228	1.611

2.5. pH studies on the RHE scale

The pH in-/dependency of OER activity is an important factor that provides valuable mechanistic insight into the degree of concertedness of PCET, reaction orders, and intermediates. To maintain consistency in the thermodynamic driving force across various pH levels, the results were compared on the RHE scale. The pH-independency on the RHE scale traditionally indicates the concertedness of H^+/e^- transfer in metal-based OER electrocatalysts [2], while the degree of pH-dependency reflects a degree of non-concertedness during the PCET process [2, 3]. The electrochemical measurements were respectively carried out on GR, GO-CPTMS-THPP, Shell-I, and Shell-II in a narrow pH range of 12.5 to 13.7 (Figures 6A–C). The varying relative pH dependency of voltammograms reveals different degrees of non-concertedness during PCET. Due to the absence of metallic cations in the PCET catalyst body, the results did not show the conventional pure concertedness behavior in the PCET process observed on metallic substrates [2]. It seems that the identity of the catalytic platform (metallic or non-metallic), apart from the OER yield, directly governs the concertedness or non-concertedness of PCET. Regardless of the magnitude of the current density, depending on whether the substrate is metallic or non-metallic, the PCET reaction can proceed along either concerted or non-concerted pathways. For instance, the presence of different functional groups such as OH and COOH on graphite, although exhibiting the lowest efficiency, slightly alters the PCET pathway toward a non-concerted process. Therefore, it manifests as a slight distinction in the voltammograms recorded on the RHE scale. A superior degree of non-concertedness is observed for Shell-II, correlating with higher catalytic activity. A similar behavior was observed in our previous study, where the single-crystalline zwitterionic hydrogen-bonded organic framework (ZHOF), as a metal-free interface, clearly separated the LSVs on the RHE scale [3]. The reaction orders, calculated from the slope of the plot of log J vs pH (Fig. 6A–C) over the potential range

of 1.75 to 1.90 V, show values ranging from 0.41 to 0.94. These fractional non-zero reaction orders suggest an n-CPET process in which protons play a role in complex reaction networks and associated elementary steps.

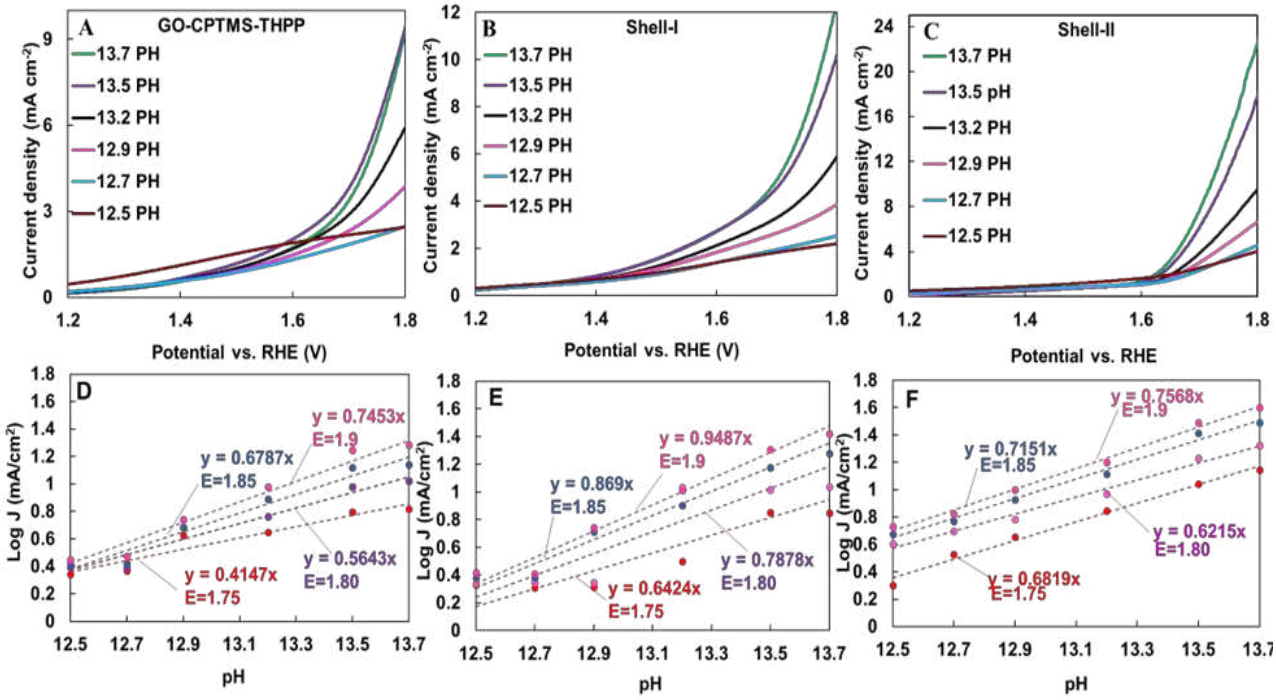


Fig. 6. pH-dependent OER activity on RHE scale. LSV curves over the pH range of 12.5 to 13.7 for (A) GO-CPTMS-THPP (B) Shell-I (C) Shell-II. (D, E and F) The plot of Log J vs. pH exhibits fractional reaction orders of 0.41-0.94 at different overpotentials.

2.6. Electrochemical impedance spectroscopy (EIS) study

Electrochemical impedance spectroscopy (EIS) measurements were performed in 0.1 M KOH with an AC amplitude of 5 mV under DC operating conditions and over a frequency range of 10 kHz to 0.01 Hz. The Nyquist plot displays a semicircle in the low-frequency region, although it continues through a 45° transmission line toward the high-frequency region instead of turning to the horizontal axis. The 45° transmission line in the high-frequency region implies an anomalous diffusional regime perturbed by a kinetically dominant exchange reaction at the electrode–electrolyte interface (Fig. 7A). The observed G impedance features a combination of Warburg behavior at high frequency and a reaction arc at low frequency, characteristic of semi-infinite diffusion–reaction coupling. It indicates recurrent chemical (exchange) reactions between protonic species and COS residues occurring both before and after the electrochemical step. The finite-length Warburg (FLW) and Gerischer impedance (G) models are considered for TLM

depending on the competitive rates of diffusion processes and interfacial exchange reactions. The appearance of G expresses a predominant chemical reaction governing mass transport at the electrode–electrolyte interface. Meanwhile, the FLW explains a situation in which the rate of natural transport is comparable to the interfacial exchange reaction [2, 38, 39].

Figure 7A and B show the EIS study (Nyquist plots of non-metal-modifier-based proton relay systems) of (A) GR, (B) GO, (C) GO-CPTMS-THPP, (D) 'GO-CPTMS-THPP-MBA, (E) Shell-I, and (F) Shell-II in 0.1 M KOH at the operational DC potential of OER. The bare graphite shows a charge-transfer resistance (Rct) of ca. 600 Ω (curve A). The Rct decreases to 400 Ω for GO (curve B), suggesting facilitated interfacial charge transport. GO contains abundant oxygen-containing functional groups (hydroxy/epoxy on the basal plane and hydroxy on the edges) that may participate in PT reactions [40]. Additionally, the sp^2 hybridization of GO can weaken the H-bonding of adsorbed H_2O molecules toward bulk H_2O, as indicated by the higher wavenumber of OH peaks for GO surface-adsorbed H_2O compared to bulk H_2O (Fig. 2), reflecting weakened hydrogen-bond cooperativity. When CPTMS is loaded on GO, Rct is further increased to ca. 1000 Ω due to the blocking of active residues (Fig. not shown), hindering proton accessibility.

The attachment of THPP (curve C) reduces the OER charge-transfer resistance to around 400 Ω, indicating partial restoration of PCET activity. In curve D, the electrode experiences a further increase in Rct after linkage of MBA and disruption of PCET, highlighting the sensitivity of interfacial kinetics to molecular perturbation. When EDA (curve E) is attached, Rct drops dramatically to 164 Ω, indicating a promoted PCET reaction pathway, consistent with KIE and LSV findings. Finally, for the Shell-II electrode, the diameter of the semicircle in the Nyquist plot decreases to ca. 80 Ω, demonstrating highly efficient interfacial charge–proton coupling. The fitting curve for this electrode shows a pure Gerischer response with a Warburg slope of 45.1° at high frequency. This behavior contrasts with our recent study on a fractal-like Gerischer response with a slope of 22°, which exhibited a distinct fitting result for in-series components Cdl or CPE. The pure G impedance does not depend on either in-series component, Cdl or CPE (Fig. 7B), confirming a chemically dominated impedance regime.

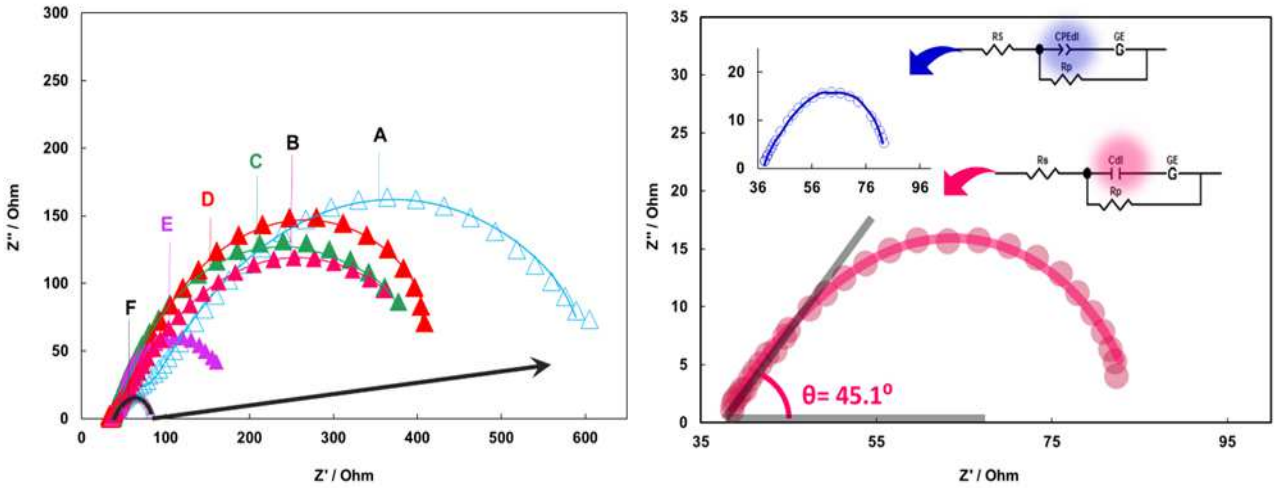


Fig. 7. Exhibiting Gerischer impedance mechanism for different substrates bearing the THPP and EDA proton relay. Left) The Nyquist plots recorded in 0.1 M KOH at (A) GR, (B) GO, (C) GO-CPTMS-THPP, (D) GO-CPTMS-THPP-MBA, (E) Shell-I and (F) Shell-II. Right) The Nyquist plot and equivalent circuit for the Shell-II describing the role of in-series components, CPE vs. C_{dl}

The stability of the as-prepared electrodes was examined through comparison of their performance during a 24 000 s electrolysis conducted in a 1.0 M KOH solution (Fig. 8). The metal-free substrates reveal exceptional stability; however, this stability was particularly pronounced for the Shell-I and Shell-II electrodes, which exhibit higher current density and severe O_2 liberation. The local accumulation of generated protons may cause damage and transformation of metallic-based electrocatalysts with traditional solution-based proton scavengers [26, 41], whereas these metal-free covalent PCET catalysts exhibit prominent stability. The Shell-II electrode, with the highest catalytic response and greatest proton liberation, demonstrates exceptional stability, with current retention of approximately 109% after 24 000 s.

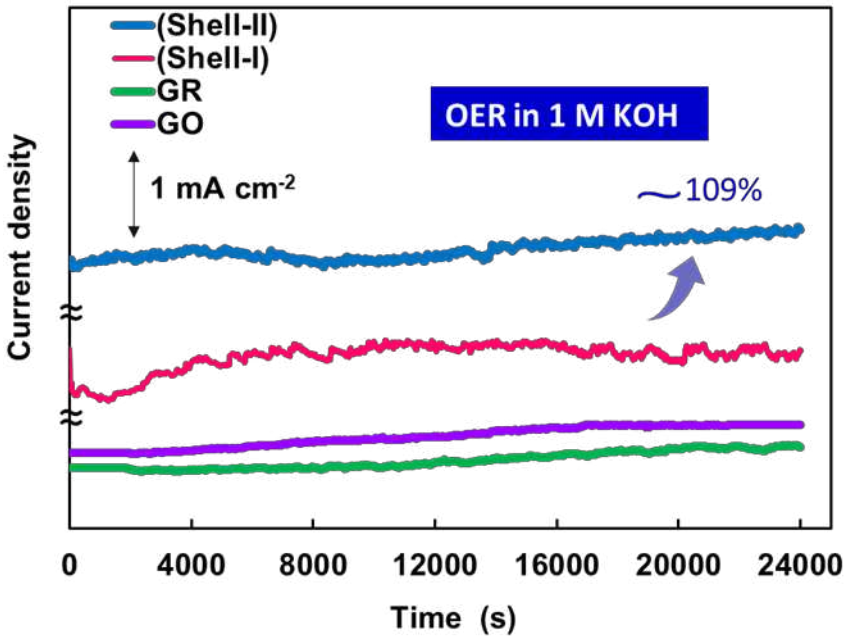


Fig. 8. Time dependence of the current density for as-synthesized COSs at constant potential 1.8 vs. RHE in 1 M of KOH.

2.7. Morphology factor and role of effective surface area

To evaluate the contribution of electrochemically active surface area (ECSA) to the observed catalytic enhancement, double-layer capacitance (Cdl) measurements were performed via cyclic voltammetry in the non-faradaic region (1.02–1.14 V vs. RHE) at scan rates of 20–160 mV s^{-1} in 1 M KOH [16, 39]. The calculated Cdl at Shell-I (3.95 $mFcm^{-2}$) and Shell-II (4.3 mF cm^{-2}) reveal a close value, reflecting the uniform morphological properties between Shel-I and II (Figure S27-29). Furthermore, the morphology factor (Φ) is considered to quantifies the relative contribution of internal versus external surface area [3]. The total differential capacitance (Cd) and its external portion (Cd, external) were evaluated through the slope values at low scan rate and high scan rate, respectively (see supporting Note 3). Using the relation of Cd=Cd, internal – Cd, external and based on the equation introduced for morphology factor ($\varphi=C_{d,internal}/C_{d,total}$) [29], an accumulative index was obtained for illustrating the role of morphology factor on the electrochemical response at both electrodes (more details on φ are in supporting Note 3).

The calculated values of φ at Shell-I and Shell-II were found to be 0.514 and 0.265, respectively. The values largely greater than 0.5 impart the greater contribution of the

inner surface area toward the external part in the electrochemical signal. The obtained φ values confirm the relatively low portion of the inner surface in the signal boosting of in Figure 3. The decreases from Shell-I (Φ = 0.514) to Shell-II (Φ = 0.265) (Figure S24-26), demonstrates a denser covalent packing rather than proportional expansion of electrolyte-accessible sites. The slight difference in φ value confirms a negligible difference between the morphological factors on the electrochemical activities of Shell-I and Shell-II.

2.8. Proposed PCET Mechanism

Based on kinetic isotope effects, Tafel analysis, proton inventory studies, and Gerischer impedance study, we propose a non-concerted PCET mechanism for the OER on Shell-II in alkaline media. As an integrated proton-relay system, the focal pyrrolic nitrogens bind hydroxide/water substrates, while terminal EDA amines facilitate rapid proton shuttling via a strong HBN. This architecture enables a four-electron OER pathway producing O_2, with the first electron transfer serving as the RDS, consistent with the observed Tafel slope of 123 mV dec^{-1} and secondary KIE (~1.0). Critically, the exchange rate of protons through this relay exceeds natural diffusion, as evidenced by pure Gerischer impedance behavior, thereby preventing local acidification and enabling stable high-current operation even in neutral media, all experimental evidences are listed in the Table 2 in following:

Step 0 (Pre-equilibrium – H-bond network organization):

$4\ OH^-(aq) + COS\text{-}(NH_2)_4 \rightleftharpoons [COS\text{-}(NH_2\cdots OH^-)_4]$

Step 1 (RDS – First electron transfer, no O–H cleavage):

$[COS\text{-}(NH_2\cdots OH^-)_4] \rightarrow [COS\text{-}(NH_2\cdots OH^{\bullet})_4] + e^-$ (k_1, rate-determining)

Step 2 (Proton hopping via relay network):

$[COS\text{-}(NH_2\cdots OH\bullet)_4] + 2\ COS\text{-}NH_2 \rightarrow [COS\text{-}(NH_3^+\cdots O\bullet)_2\cdots(NH_2\cdots OH\bullet)_2]$

Step 3 (Second electron transfer + O–O coupling):

$[COS\text{-}(NH_3^+\cdots O\bullet)_2\cdots(NH_2\cdots OH\bullet)_2] \rightarrow [COS\text{-}(NH_3^+\cdots O\text{–}O\bullet)_2] + 2e^- + 2H_2O$

Step 4 (Third/fourth electron transfers + O_2 release):

$[COS\text{-}(NH_3^+\cdots O\text{–}O\bullet)_2] \rightarrow COS\text{-}(NH_2)_4 + O_2\uparrow + 2e^-$

Table 2. Critical mechanistic evidence supporting the proposed PCET pathway.

Experimental Observation	Mechanistic Implication	Ref.
Secondary KIE (KIE ≈ 1.0)	No O–H cleavage in RDS; PT precedes ET	[33]
Tafel slope = 123 mV dec^{-1}	First ET step as RDS (α ≈ 0.5, n = 0)	[2, 30]
Gerischer impedance (45° Warburg) in high frequencies	Chemical exchange (proton hopping) >> natural diffusion of protonic species	[2]
Fractional reaction orders (0.41–0.94) in pH studies and Z effect=1.611	Non-concerted PCET with multiple protonic sites	[32, 42]
Non-concerted PCET (pH-dependent on RHE)	PT and ET occur in separate steps, OH^- deprotonation requires explicit PT to amine relays before ET	[32, 42]
Mg^{2+} blocking effect	Focal pyrrolic N essential for OH^- binding, Mg^{2+} coordinates pyrrolic N, preventing OH^- adsorption → activity abolished	[33]
ϕ = 0.228 (<0.25)	Strong H-bonding stabilizes $OH^{-}\cdots N$ transition state, Low ϕ indicates single-well potential for H^+ between OH^- and N sites	[9, 36]

2.9. Comparison of OER Performance

To benchmark the catalytic efficacy of the Shell-II electrode, Table 3 summarizes a comparative analysis of OER performance metrics against representative state-of-the-art metal-free electrocatalysts.

Table 3. Comparison of OER performance between Shell-II and representative metal-free electrocatalysts

Catalyst	Electrolyte	η @ 10 mA cm^{-2} (mV)	Tafel Slope (mV dec^{-1})	Stability (h / current retention)	Ref.
Shell-II (This work)	1.0 M KOH & Neutral (pH≈7)	320	123	6.7 h / 109%	—
N,P-co-doped carbon foam	0.1 M KOH	390	85	10 h / ~95%	[1]
Free-base porphyrin polymer	1.0 M KOH	520	131.5	>60 h	[14]
Thiadiazole-based COF	1 M KOH	320	39	>11 h	[16]
Zwitterionic H-bonded framework (ZHOF)	1 M KOH	255	158	10 h / 102%	[3]
Guanidinium-terminated polymer	1 M KOH	183	113	>8h (>96% current retention)	[2]
Donor–acceptor COF	1.0 M KOH	398	89	>18 h	[43]
Polymer-functionalized GO	1.0 M KOH	240	47	>10 h	[44]
L-Lysine-Functionalized rGO	1.0 M KOH	330	80	>10 h	[39]
Polymeric proton relay:	1.0 M KOH	230	120	>14 h	[42]
3D honeycomb porous sulfonated covalent organic polymer (PCOP)	0.1 M of KOH	234	165	Excellent stability reported	[45]

3. Conclusions

The focal and prepositioned terminal amines within GO-bonded COS contribute through H-bonding to the fast pre- and post-exchange reactions during OER. The exchange reaction rate surpassed the natural transport within the diffusion layer, as experimentally supported by the extended case of TLM, showing **a** non-depressed pure Gerischer response. This factor is partly counterbalanced by the requirement, resulting from the overall stabilization, to inject an electron during electrocatalysis. Thanks to the exchange reaction on the Lewis base amine sites, PCET proceeds through downhill PT, as studied via KIE and proton inventory studies. The SKIE (KIE ≈ 1) indicates no PT participation in the RDS of PCET, where a Tafel slope around the theoretical value of 118 mV dec^{-1} suggests the first ET step of the OER as the RDS. The results of isotopic and G-impedance studies demonstrate that the two-type amine-rich COS plays the role of H-bonding stabilizers and high-concentration proton exchangers. The stabilization role of the GO/COS platform via strong H-bonding, with a zero-point energy located below the top of the barriers, separates the formed intermediates from the initial and final equilibrium configurations, owing to the non-concertedness revealed through pH studies on the RHE scale. It is also remarkable that the cooperative property of these two types of amines may be decisive, where the terminal amines, despite their tremendous effect in PT, lose their effectiveness following the inactivation of the focal amines upon Mg(II) inclusion. For the first time, we studied the possible agitation of water's HBN through the interfacial collaring of COS with water clusters, which increases the portion of single HB toward triply hydrogen-bonded OH groups for successful substrate adsorption during WOR.

Supporting Information

Supporting Information is available from the authors

Acknowledgments

The authors gratefully appreciated the financial support of this work by the research council of Razi university.

Data availability

All other data are available from the corresponding author upon reasonable request.

Funding

Our research did not receive any dedicated funding from external agencies or grants. The only support we received was the official assistance from our institution's Research Deputy, which was solely used to cover the costs of the characterization.

4. References

[1] Zhang, J., Zhao, Z., Xia, Z. & Dai, L. A metal-free bifunctional electrocatalyst for oxygen reduction and oxygen evolution reactions. *Nat. Nanotechnol*. **10** (5), 444-452 (2015).

[2] Shamsipur, M., Ardeshiri, M., Taherpour, A. A. & Pashabadi, A. Unveiling the mechanistic implications of water oxidation reactions boosted by guanidine proton relays: a chemical-electrochemical-chemical pathway and a non-concerted proton-electron transfer. *J. Mater. Chem. A*. **9** (5), 2937-2947 (2021).

[3] Azizi, R., Shamsipur, M., Taherpour, A. A. & Pashabadi, A. Zwitterionic hydrogen-bonded organic framework (ZHOF): a metal-free water oxidation proton relay in alkaline and neutral media. *J. Mater. Chem. A*. **11** (3), 1491-1502 (2023).

[4] Shamsipur, M. & Pashabadi, A. What Can be Learned from Proton Relays in Photosystem II toward Complete Biomimicking of Oxygen Evolution Reaction Electrocatalysis? *ChemElectroChem*. **10** (24), e202300423 (2023).

[5] Shamsipur, M. & Pashabadi, A. Latest advances in PSII features and mechanism of water oxidation. *Coord. Chem. Rev*. **374**, 153-172 (2018).

[6] Shamsipur, M. & Pashabadi, A. What has biomimicry so far brought on mysterious natural oxygen evolution? *Coord. Chem. Rev*. **401**, 213068 (2019).

[7] Umena, Y., Kawakami, K., Shen, J. R. & Kamiya, N. Crystal structure of oxygen-evolving photosystem II at a resolution of 1.9 Å. *Nature*. **473** (7345), 55-60 (2011).

[8] Savéant, J. M. Proton relays in molecular catalysis of electrochemical reactions: Origin and limitations of the boosting effect. *Angew. Chem. Int. Ed.* **58** (7), 2125-2128 (2019).

[9] Li, W., Li, F., Yang, H., Wu, X., Zhang, P., Shan, Y. & Sun, L. A bio-inspired coordination polymer as outstanding water oxidation catalyst via second coordination sphere engineering. *Nat. Commun.* **10** (1), 5074 (2019).

[10] Sitko, R., Turek, E., Zawisza, B., Malicka, E., Talik, E., Heimann, J. & Wrzalik, R. Adsorption of divalent metal ions from aqueous solutions using graphene oxide. *Dalton Trans*. **42** (16), 5682-5689 (2013).

[11] Hajian, R., Fung, K., Chou, P. P., Wang, S., Balderston, S. & Aran, K. Properties and applications of functionalized graphene oxide. *Mater. Matters*. **14**, 1-15 (2019).

[12] Guo, S., Garaj, S., Bianco, A. & Ménard-Moyon, C. Controlling covalent chemistry on graphene oxide. *Nat. Rev. Phys*. **4** (4), 247-262 (2022).

[13] Karousis, N., Sandanayaka, A. S., Hasobe, T., Economopoulos, S. P., Sarantopoulou, E. & Tagmatarchis, N. Graphene oxide with covalently linked porphyrin antennae: Synthesis, characterization and photophysical properties. *J. Mater. Chem.* **21** (1), 109-117 (2021).

[14] Ge, Y., Lyu, Z., Marcos-Hernández, M. & Villagrán, D. Free-base porphyrin polymer for bifunctional electrochemical water splitting. *Chem. Sci.* **13** (29), 8597-8604 (2022).

[15] Taranu, B. O. & Fagadar-Cosma, E. Catalytic properties of free-base porphyrin modified graphite electrodes for electrochemical water splitting in alkaline medium. *Processes*. **10** (3), 611 (2022).

[16] Mondal, S., Mohanty, B., Nurhuda, M., Dalapati, S., Jana, R., Addicoat, M., Datta, A., Jena, B. K. & Bhaumik, A. A thiadiazole-based covalent organic framework: A metal-free electrocatalyst toward oxygen evolution reaction. *ACS Catal*. **10** (10), 5623-5630 (2020).

[17] Gómez-Vidales, V., Borja-Miranda, A., Cortez-Maya, S., Amelines-Sarria, O., Rivera, M. & Martínez-García, M. Design and Synthesis of a Multi Cu (II)-porphyrin Array. *Open Chem. J*. **3** (1), 25-34 (2016).

[18] Groppo, E., Bonino, F., Cesano, F., Damin, A. & Manzoli, M. Raman, IR and INS characterization of functionalized carbon materials. (2018).

[19] Lyn, F. H., Peng, T. C., Ruzniza, M. Z. & Hanani, Z. N. Effect of oxidation degrees of graphene oxide (GO) on the structure and physical properties of chitosan/GO composite films. *Food Packag. Shelf Life*. **21**, 100373 (2019).

[20] Saputra, Q. A.; Apriany, K.; Putri, F. R.; Firdaus, M.; In IOP Conference Series*:* Materials Science and Engineering,***107***, p. 012048 (2016).

[21] Zhao, Y., Zhu, Y., Yang, G., Xia, L., Yu, F., Chen, C. & Cao, H. A pH/H_2O_2 dual triggered nanoplatform for enhanced photodynamic antibacterial efficiency. *J. Mater. Chem. B*. **9** (25), 5076-5082 (2021).

[22] Shamsipur, M., Taherpour, A. A. & Pashabadi, A. Comprehensive facilitating of water oxidation reaction by ultrasonic attenuation of hydrogen-bonded structure of water. *Ultrason. Sonochem*. **42**, 381-389 (2018).

[23] Cotugno, S., Larobina, D., Mensitieri, G., Musto, P. & Ragosta, G. A novel spectroscopic approach to investigate transport processes in polymers: the case of water–epoxy system. *Polym.* **42** (15), 6431-6438 (2001).

[24] Thouvenin, M., Linossier, I., Sire, O., Péron, J. J. & Vallée-Réhel, K. Structural and dynamic approach of early hydration steps in erodable polymers by ATR−FTIR and fluorescence spectroscopies. *Macromol*. **35** (2), 489-498 (2002).

[25] Mizuse, K. Spectroscopic investigations of hydrogen bond network structures in water clusters. *Springer Science & Business Media*, (2013).

[26] Ahanjan, K., Shamsipur, M., Hassani, N., Neek-Amal, M. & Pashabadi, A. Oxygen Vacancy-Originated Inorganic Proton Relay for the Oxygen Evolution Reaction: Fast Proton Hopping via La-Doped Praseodymium Carbonate Hydroxide. *J. Phys. Chem. C*. **127**, 24508-24522.35 (2023).

[27] Ge, Y., Lyu, Z., Marcos-Hernández, M. & Villagrán, D. Free-base porphyrin polymer for bifunctional electrochemical water splitting. *Chem. Sci.* **13** (29), 8597-8604 (2022).

[28] Ge, Y., Lyu, Z., Marcos-Hernández, M. & Villagrán, D. Free-base porphyrin polymer for bifunctional electrochemical water splitting. *Chem. Sci*. **13** (29), 8597-8604 (2022).

[29] Ahanjan, K., Shamsipur, M., Taherpour A. A. & Pashabadi, A. Catalytic synergism in Mn-heterostructured molybdenum oxysulfide hybridized with transition metal phosphides: A robust amorphous water oxidation catalyst. *Electrochim. Acta*. **433**,141249 (2022).

[30] Fang, Y. H. & Liu, Z. P. Tafel kinetics of electrocatalytic reactions: from experiment to first-principles. *ACS Catal*. **4** (12), 4364-4376 (2014).

[31] Li, W., Li, F., Yang, H., Wu, X., Zhang, P., Shan, Y. & Sun, L. A bio-inspired coordination polymer as outstanding water oxidation catalyst via second coordination sphere engineering. *Nat. Commun.* **10** (1), 5074 (2019).

[32] Hammes-Schiffer, S. Proton-coupled electron transfer: Moving together and charging forward. *J. Am. Chem. Soc*. **137** (28), 8860-8871 (2015).

[33] Costentin, C., Passard, G., Robert, M. & Savéant, J. M. Pendant acid–base groups in molecular catalysts: H-bond promoters or proton relays? Mechanisms of the conversion of CO_2 to CO by electrogenerated iron (0) porphyrins bearing prepositioned phenol functionalities. *J. Am. Chem. Soc*. **136** (34), 11821-11829 (2014).

[34] Kreevoy, M. M., Liang, T. M. & Chang, K. C. Structures and isotopic fractionation factors of complexes AHA-1. *J. Am. Chem. Soc*. **99** (15), 5207-5209 (1977).

[35] Venkatasubban, K. S. & Schowen, R. L. The Proton Inventory Techniqu. *Crit. Rev. Biochem.* **17** (1), 1-44 (1984).

[36] Kohen, A. & Limbach, H. H. Isotope effects in chemistry and biology. *CRC Press.* (2005).

[37] Kreevoy, M. M. & Liang, T. M. Structures and isotopic fractionation factors of complexes, A1HA2. *J. Am. Chem. Soc.* **102** (10), 3315-3322 (1980).

[38] Nguyen, T. Q. & Breitkopf, C. Determination of diffusion coefficients using impedance spectroscopy data. *J. Electrochem. Soc*. **165** (14), E826-E831 (2018).

[39] Sapner, V. S., Chavan, P. P. & Sathe, B. R. L-Lysine-functionalized reduced graphene oxide as a highly efficient electrocatalyst for enhanced oxygen evolution reaction. *ACS. Sustain. Chem. Eng*. **8** (14), 5524-5533 (2020).

[40] Wu, L. & Jiang, X. Proton transfer at the interaction interface of graphene oxide. *Anal. Chem.* **90** (17), 10223-10230 (2018).

[41] Huo, Q., Cao, J., Mi, L., Shao, J., Lv, M., Chen, X. & He, C. A robust strategy to boost the proton transfer of heterogeneous catalysts for efficient and sustainable water oxidation towards practical applications. *J. Mater. Chem. A*. **11** (3), 1335-1342 (2023).

[42] Ahanjan, K., Shamsipur, M. & Pashabadi, A. Water oxidation on a sustainable polymeric proton relay: the role of post-phosphating of an oxide sub-layer on PCET. *Nanoscale* **17** (10), 5798-5811 (2025).

[43] Prakash, K., Ahmed, I., Deka, R. & Mobin, S. M. Metal free donor–acceptor covalent organic frameworks as efficient electrocatalysts for oxygen evolution reaction. *J. Mater. Chem. A*. **13**, 30214–30223 (2025).

[44] Ghouri, Z. K., Elsaid, K., Badreldin, A., Nasef, M. M., Che Jusoh, N.W. & Abdel-Wahab, A. Enhanced oxygen evolution reaction on polyethyleneimine functionalized graphene oxide in alkaline medium. *Mol. Catal*. **516**, 111960 (2021).

[45] Azizi, R., Shamsipur, M., Taherpour, A., Miri, M. & Pashabadi, A. 3D honeycomb porous sulfonated covalent organic polymer (PCOP) synthesized on carbon fabric at refrigerated temperature: supercapacitor and metal-free proton relay for water oxidation in alkaline and neutral media. *Mater. Adv.* **6**, 6094–6108 (2025).

Supplementary Files

This is a list of supplementary files associated with this preprint. Click to download.

- revisedSupportinginformation.docx